

# Chapter 16

## Acoustic Diagnosis Device for Dentistry

**Kouki Hatori, Yoshifumi Saijo, Yoshihiro Hagiwara, Yukihiro Naganuma, Kazuko Igari, Masahiro Iikubo, Kazuto Kobayashi, and Keiichi Sasaki**

**Abstract** There are a lot of diseases which show the abnormal elastic property. Although many medical doctors and dentists have noticed the change of tissue elasticity due to the disease, the diagnostic device to examine the tissue elastic property objectively has not well developed.

At Tohoku University, acoustic microscopy (AM) for medicine and biology has been developed and applied for more than 20 years. Application of AM has three major features and objectives. First, specific staining is not required for characterization or observation. Second, it provides the elastic property and information of

---

K. Hatori (✉)

Department of Prosthodontics, Matsumoto Dental University,  
1780 Gobara Hirooka, Shiojiri, Nagano 399-0781, Japan

Division of Advanced Prosthetic Dentistry, Tohoku University Graduate School of Dentistry,  
4-1 Seiryō-machi, Aoba-ku, Sendai, Miyagi, Japan

e-mail: [khat810@yahoo.co.jp](mailto:khat810@yahoo.co.jp)

Y. Saijo

Biomedical Imaging Laboratory, Graduate Schools of Biomedical Engineering and Medical Sciences, Tohoku University, Sendai, Miyagi, Japan

Y. Hagiwara

Department of Orthopaedic Surgery, Tohoku University, Tohoku University School of Medicine, Sendai, Miyagi, Japan

Y. Naganuma

Division of Advanced Prosthetic Dentistry, Tohoku University Graduate School of Dentistry,  
4-1 Seiryō-machi, Aoba-ku, Sendai, Miyagi, Japan

Dentistry for the Disabled, Tohoku University Hospital, Sendai, Miyagi, Japan

K. Igari

Dentistry for the Disabled, Tohoku University Hospital, Sendai, Miyagi, Japan

M. Iikubo

Department of Oral Diagnosis, Tohoku University Graduate School of Dentistry,  
Sendai, Miyagi, Japan

K. Kobayashi

Honda Electronics Co. Ltd., Toyohashi, Aichi, Japan

K. Sasaki

Division of Advanced Prosthetic Dentistry, Tohoku University Graduate School of Dentistry,  
4-1 Seiryō-machi, Aoba-ku, Sendai, Japan

the subject, because acoustic properties have close correlation with the mechanical property of the subject. Third, it makes the observation easy and rapid. The purpose of this study is to observe carious dentin and periodontal ligament (PDL) using AM. Moreover, I would like to propose the prototype of the portable caries detector.

AM clearly visualizes the color distribution of the acoustic properties of the subject.

The acoustic examination device may be a powerful apparatus not only to visualize the morphological appearance but also to diagnose the disease.

**Keywords** Acoustic imaging • Human teeth • Dentin caries • Periodontal ligament • Diagnosis

## 16.1 Introduction

We have been developing a scanning acoustic microscope (SAM) system at Tohoku University since 1985. SAM has been applied to observe the acoustic properties of various cells, organs, and disease state: vein endothelial cells, gastric cancer, normal kidney and renal cancer, infarcted myocardium, atherosclerosis of aorta and carotid arterial plaques, etc. In biomedical study, the application of SAM is useful for the intraoperative pathological examination, the observation of low-frequency ultrasonic images, and the assessment of biomechanical properties at a microscopic level [1–11]. The application of SAM in biomedical study has two major features and objectives. First, the specific staining is unnecessary for observation. Second, SAM provides the acoustic properties and information such as the acoustic intensity, the sound speed propagating in the sample, and the acoustic attenuation. Therefore, SAM enables to acquire the elastic property of the subject and the quantitative values of the acoustic properties, because the acoustic properties have close correlation with the mechanical property of the subject. After 2004, the third advantage to use SAM was added, which is that SAM makes the observation easy and rapid. One scanning takes 2 min approximately using new concept SAM, because new concept SAM system was developed using a single-pulsed wave instead of continuous waves used in the conventional SAM system in 2004 [12, 13]. Sano et al. reported that the decalcification during tissue preparation did not alter the sound speed propagating in fibrocartilage or bone [14]. Hagiwara et al. reported that the sound speed propagating in the posterior synovial membrane after knee joint contracture increased significantly using decalcified specimen [13]. These reports indicate that the decalcified specimen is also appropriate to observe the acoustic properties using SAM.

Periodontal ligament (PDL) is the dense fibrous connective tissue which binds the root cementum to the alveolar bony socket. This tissue is especially cellular and vascular tissue and plays pivotal role to develop and maintain periodontal membrane. PDL supports and dissipates the occlusal force and regulates the tooth eruption. Thus, PDL performs these important oral functions [15, 16]. Since many studies of the mechanical properties of PDL have been reported using animal model

[17], it was pointed out that mechanical properties of PDL showed the values (0.9–1.6 N/mm<sup>2</sup>) in the extrusion testing in rat mandibular first molar [18, 19]. These reports were the dynamic tests for the measurement of the mechanical properties of PDL, but little is known about the static test for the measurement of the mechanical properties of PDL in vivo. In this paper, the first purpose is to observe the rat PDL using SAM.

Acoustic impedance, which is given as a product of sound speed and density, has a close correlation with the elastic modulus, when the value of density of the embedding material was constant. Based on the above background, HONDA ELECTRONICS Co., Ltd. (Toyohashi, Japan) and Tohoku University Graduate School of Biomedical Engineering have developed the acoustic impedance microscope (AIM) which enables to image the two-dimensional distribution of the acoustic intensity and impedance of the sample [20]. AIM has been applied to observe cerebellum tissue [21] and cultured glial and glioma cells [22]; these studies reported that AIM also provided the acoustic intensity and impedance image at a microscopic level.

Dental caries is a common and chronic disease in oral cavity and results from the production of acid by caries-inducing bacterial fermentation on the tooth surface. The acid by caries-inducing bacterial metabolism causes the decalcification of the hard tissues of the teeth such as enamel and dentin [23]. Finally the decalcified lesion becomes soft and is recognized as dental caries. Dental caries cause the change of hardness of the teeth [24, 25]. The change of acoustic properties of dentin caries has not been observed using AIM yet. In this paper, the second purpose is to observe the human dentin caries using AIM and to observe the microstructure of the human dentin caries using the scanning electron microscope (SEM).

Based on these the technology of producing such acoustic imaging devices, HONDA ELECTRONICS Co., Ltd. and Tohoku University Graduate School of Biomedical Engineering fabricated a prototype of portable acoustic stiffness checker. In this paper, the last purpose is to introduce about this acoustic stiffness checker.

## 16.2 Materials and Methods

### 16.2.1 *Observation of Rat Periodontal Ligament Using Scanning Acoustic Microscopy*

#### 16.2.1.1 Scanning Acoustic Microscope (SAM)

The sound speed propagating in a solid substance is defined as:

$$C = \sqrt{\frac{E(1-\delta)}{\rho(1-2\delta)(1+\delta)}} \quad (16.1)$$

where  $C$  is the sound speed propagating in the object,  $E$  is the Young's modulus of the object,  $\rho$  is the Poisson's ratio, and  $\delta$  is the density of the object. Thus, it is

implied that the change of the sound speed propagating in the tissue is the change of the tissue elastic property [26]. The Young's modulus ( $E$ ) is in proportion to the square of the sound speed; in the other words, the change of the sound speed provides with the information of the change of material hardness. The observation of the sound speed propagating in the thin sliced sample enables us to understand the proper hardness of the thin sliced sample [14].

Our SAM is mainly composed of five units: (1) ultrasonic transducer with acoustic lens, (2) pulse generator, (3) digital oscilloscope with system control PC (Windows), (4) stage control microcomputer, and (5) display monitor (Figs. 16.1 and 16.2). The emission of the electric pulse was within 400 ps from excitation, and the pulse voltage was 40 V. A single-pulsed ultrasonic impulse with a pulse width of 5 ns was generated and received by the same ultrasonic transducer above the section. The aperture diameter of the ultrasonic transducer was 1.2 mm, and the focal length was 1.5 mm (Fig. 16.3). The central frequency was 80 MHz, the nominal bandwidth was 50–105 MHz (–6 dB), and the pulse repetition rate was 10 kHz. Taking the focal distance and the sectional area of the transducer into consideration, the diameter of the focal spot was estimated as 20  $\mu\text{m}$  at 80 MHz. Physiologic saline was used as the coupling medium between the transducer and the section. An ultrasonic wave with a wide frequency component was generated by applying the voltage pulse of 40 V and was irradiated to the section on the glass slide. The reflections from the section surface and those from interface between the section and the glass slide were detected by the transducer and were introduced into the digital oscilloscope (TDS 5052, Tektronix Inc., Portland, USA). The band limit was 300 MHz, and the sampling rate was 2.5 GS/s. In order to reduce random noise, four times of pulse responses at the same point were averaged in the digital oscilloscope prior to being introduced into the computer.

The transducer was mounted on an X-Y stage driven by the stage control microcomputer which was operated by the system control PC via an RS232C. The X- and Y-scan were operated by a linear servo motors by the incoming signal from stage control circuit.

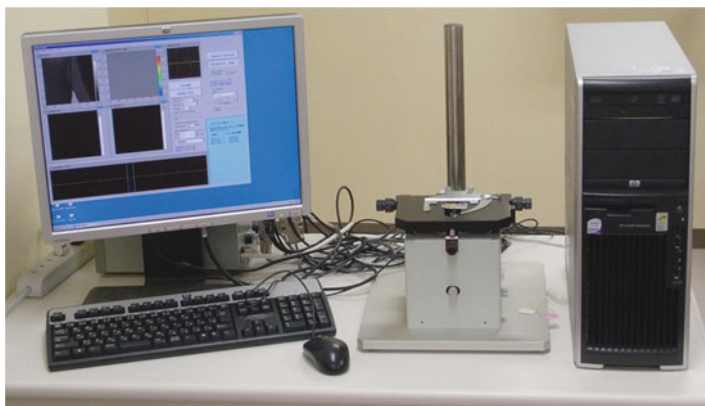


**Fig. 16.1** System of scanning acoustic microscopy. This system can display a two-dimensional distribution of sound speed and acoustic impedance

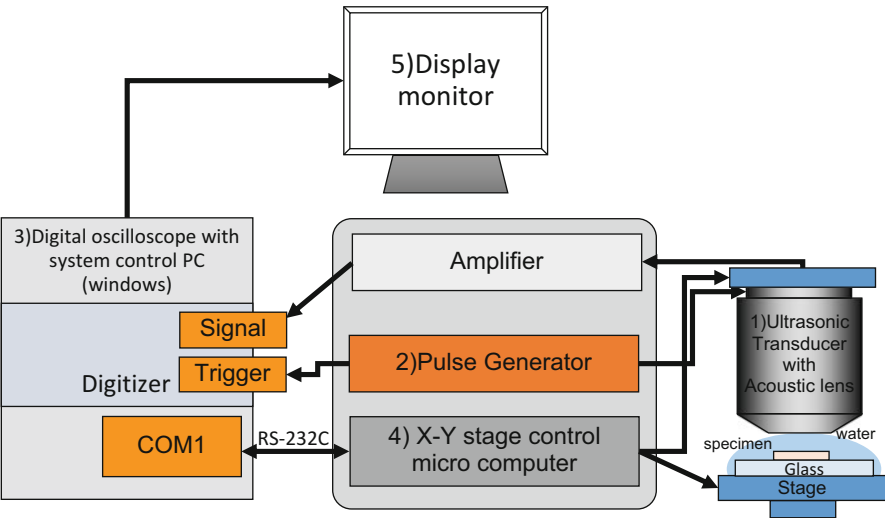
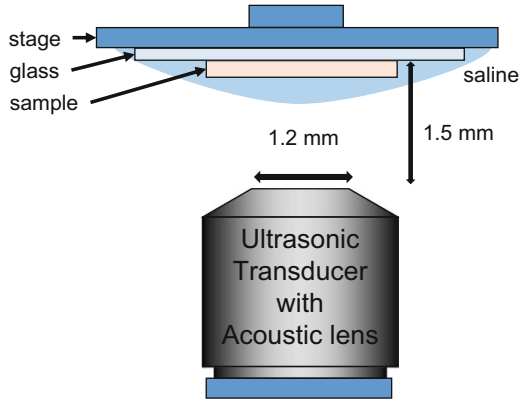
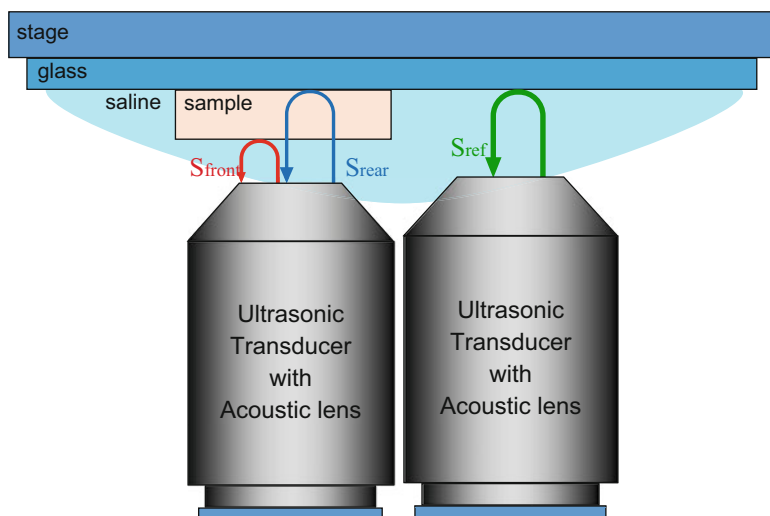


Fig. 16.2 Block diagram of scanning acoustic microscopy

Fig. 16.3 Schematic illustration of SAM transducer. The aperture diameter of the ultrasonic transducer was 1.2 mm, and the focal length was 1.5 mm. The central frequency was 80 MHz



The distance from the transducer to the glass surface was 1.5 mm. Reflected ultrasonic wave included three types of waveforms, which were from the surface of the section (*Sfront*), from the interface between the section and the glass (*Srear*), and the surface from the glass (*Sref*) (Fig. 16.4). The ultrasonic phases of these waveforms were standardized and recognized as a reflection wave from the glass in system control PC. Finally, two-dimensional distributions of the acoustic intensity, the sound speed, the acoustic attenuation, and the thickness of the sample of the 2.4×2.4 mm sample area were visualized with 300×300 pixels and calculated by Fourier transforming the waveform [12–14].



**Fig. 16.4** Schematic illustration of scanning image of sound speed microscope. A single-pulsed ultrasonic impulse was generated and received by the same transducer.  $S_{front}$  is the reflection from the surface of the section,  $S_{rear}$  is the reflection from the interface between the section and the glass, and  $S_{ref}$  is the reflection the surface from the glass

### 16.2.1.2 Tissue Preparation

The protocol for this experiment was approved by the Animal Research Committee of Tohoku University (approval number: 22–24).

A total of 28 male Wistar rats at 3-, 5-, 7- and 10-week-old postnatally were used in this study. Twenty-eight rats were prepared for SAM analysis (3-, 5-, 7- and 10-week-old;  $n=7$ /each age).

The rats were generally anesthetized with intraperitoneal injection of pentobarbital sodium (30 mg/kg body weight) (Somnopenyl®; Kyoritsu Seiyaku, Tokyo, Japan) and fixed with 4% paraformaldehyde (PFA) in 0.1 M phosphate buffered saline (PBS) (pH7.4) by perfusion through the aorta. The mandibles were resected and immersed in the same fixative overnight at 4 °C. The fixed specimens were decalcified in 10% ethylenediaminetetraacetic acid (EDTA) in 0.01 M PBS (pH7.4) for 6 weeks at 4 °C. After dehydration through a graded series of ethanol solution, the specimens were embedded in paraffin and finally cut into 5- $\mu$ m sagittal (mesiodistal) sections from the buccal to the lingual side of the mandible. Standardized serial sections were made in the medial periodontal space region of the lower first molar.

### 16.2.1.3 Image Analysis

Normal light microscope (DM3000, LEICA, Wetzlar, Germany) was used to take the microscopic images corresponding to the stored SAM images. A region of observation by SAM was set in the interradicular region (IRR) and the mesial

radicular region (MRR) of PDL in each section (Fig. 16.5). SAM images with a gradation color scale were acquired to visualize the clear distribution of the sound speed. In order to calculate the sound speed propagating in PDL, the color SAM images were processed for the gray scale images by the same SAM system. Finally, in the observed region, the sound speed propagating in PDL, excluding cementum, dentin, and alveolar bone, was calculated using commercially available image analysis software (PhotoShop 7.0, Adobe Systems Inc., San Jose, CA, USA).

### 16.2.1.4 Statistics

Data in each PDL region were analyzed using one-way factorial analysis of variance (ANOVA) with Tukey's post hoc multiple comparisons. Differences between IRR and MRR at each rat age were analyzed using paired *t*-test. All data were expressed as the mean  $\pm$  SD. A value of  $p < 0.05$  was accepted as statistically significant.

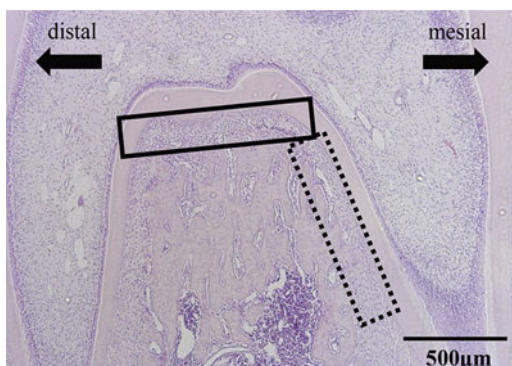
## 16.2.2 Observation of Human Carious Dentin Using Acoustic Impedance Microscopy

### 16.2.2.1 Acoustic Impedance Microscope (AIM)

Acoustic impedance mode was applied for visualization and observation of sample surface. The acoustic impedance of a material is defined as a product of the density and the sound speed. The acoustic impedance of physiological saline is used to verify the calibration curve in the following equation in its simplest form [22]:

$$Z = \rho c \quad (16.2)$$

**Fig. 16.5** Histological appearance of PDL of the first molar of rat mandible. Interradicular region (IRR) area is encircled by the black solid rectangle. Mesial radicular region (MRR) is encircled by the black dotted rectangle. 5 $\times$  original magnification. Bar = 500  $\mu$ m



where  $Z$  is acoustic impedance,  $\rho$  is density, and  $c$  is sound speed.

The acoustic approach should provide the information of the elastic bulk modulus because the relationship among the sound speed, the density, and the elastic bulk modulus of the material is described in the following equation in its simplest form:

$$C = \sqrt{\frac{K}{\rho}} \quad (16.3)$$

where  $C$  is sound speed,  $K$  is elastic bulk modulus, and  $\rho$  is density [27].

Taken together these equations, the elastic bulk modulus is described in the following equation:

$$K = Z^2 / \rho \quad (16.4)$$

where  $K$  is elastic bulk modulus,  $Z$  is acoustic impedance, and  $\rho$  is density. Therefore, if the density of embedding material is constant, the change of acoustic impedance will indicate the change of tissue elasticity. This equation indicates that the elastic bulk modulus is in proportion to the square of the acoustic impedance. In other words, the change of the acoustic impedance indicates the change of the elastic property.

The acoustic impedance microscope (AIM) (AMS-50SI, HONDA ELECTRONICS CO., LTD, Toyohashi, Japan) in the present study was shown in Figs. 16.1 and 16.6.

An electric impulse was generated by a high-speed switching semiconductor. The start of the pulse was within 400 ps, the pulse width was 2 ns, and the pulse voltage was 40 V. The frequency of the impulse covered up to 380 MHz. The electric pulse was used to excite a transducer that had a central frequency of 300 MHz and a sapphire rod as an acoustic lens. The ultrasound spectrum of the reflected ultrasound was broad enough to cover 220–380 MHz (−6 dB). The reflections from the sample were received by the transducer and were introduced into a Windows-based PC (Pentium D, 3.0 GHz, 2 GB RAM, 250 GB HDD) via digital oscilloscope (Tektronix TDS7154B, Beaverton, USA). The frequency range was 1 GHz, and the sampling rate was 20 GS/S. Four pulse echo sequences were averaged for each scan point in order to increase the signal-to-noise ratio.

The transducer was mounted on an X-Y stage with a microcomputer board that was driven by the PC through RS232C. The both X-scan and Y-scan were driven by linear servo motors. Finally, two-dimensional distribution of the acoustic impedance was visualized and the image area was 2.4 × 2.4 mm. The total scanning takes 121 s [20].

### 16.2.2.2 Tissue Preparation

The protocols for the experiments were approved by the Ethical Committee of Tohoku University (approval number: 26–28).



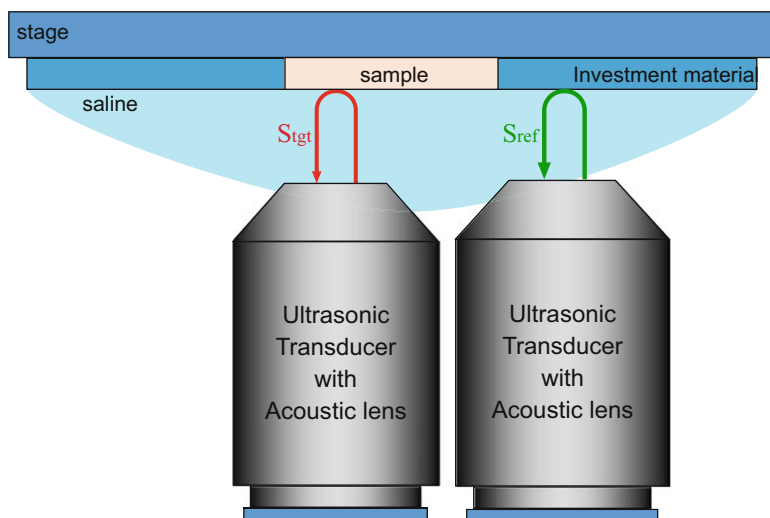


**Fig. 16.6** Schematic illustration of scanning image of the acoustic impedance microscope. *S<sub>tgt</sub>* is the reflection from the sample; *S<sub>ref</sub>* is the reflection from the investment material. In this case, substrate is water

Human molar teeth with dental caries ( $n=10$ ) were used in this study. The teeth were extracted under the diagnosis of severe periodontitis, and the extracted teeth were immediately fixed with 0.1 % glutaraldehyde and kept into the same fixative for 24 h. The teeth samples were embedded in the self-curing resin (UNIFAST III CLEAR, GC, Tokyo, Japan). The embedded samples were cut sagittally by saw microtome (SP1600, LEICA, Wetzlar, Germany) perpendicular to the caries surface, and the sliced sections (sagittal sections) were polished and smoothened with waterproof abrasive papers (#1000 and #2000) (Fig. 16.7). The thickness of polished section was 400–600  $\mu\text{m}$ . The prepared sections were assessed by AIM and the scanning electron microscope (SEM), respectively.

### 16.2.2.3 Scanning Electron Microscopy (SEM)

After the acoustic microscopic observation, the scanning electron microscopic investigation for the carious dentin lesion and the sound dentin area was carried out in order to observe the microstructural surface of both the carious lesion and the sound dentin area. The polished samples for SEM observation were initially air-dried and mounted on aluminum stubs. The sample was sputtered with a 20- $\mu\text{m}$ -thickness of carbon film layer (JFC-1100, JEOL Ltd., Tokyo, Japan) and then analyzed with SEM (JSM-6060, JEOL Ltd., Tokyo, Japan). The accelerating voltage was 15 kV and the specimen irradiation current was 1.0 nA at SEM examination.

**Fig. 16.7** Sliced human molar teeth with dental caries. Dentin caries is encircled by the *red dotted rectangle*, and sound dentin is encircled by the *black dotted rectangle*



#### 16.2.2.4 Statistics

Differences between the dentin caries and the sound dentin were analyzed using paired *t*-test. All data were expressed as the mean  $\pm$  SD. A value of  $p < 0.05$  was accepted as statistically significant.

### 16.2.3 Portable Acoustic Stiffness Checker (PASC)

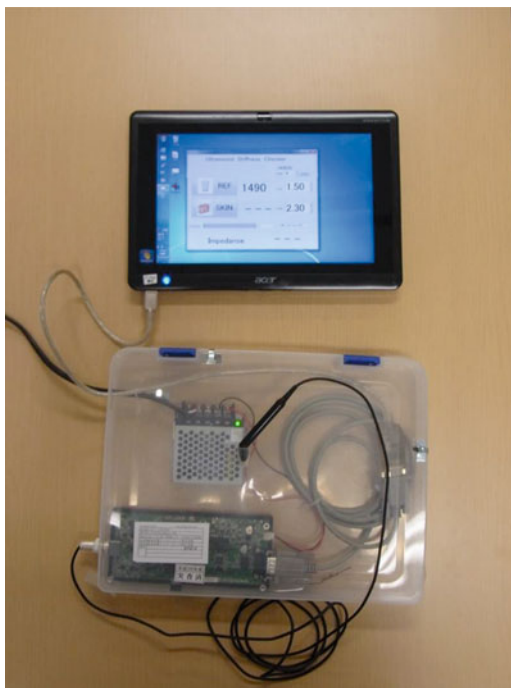
A prototype of portable acoustic stiffness checker was shown in Fig. 16.8. Our PASC is mainly composed of three units: (1) acoustic probe, (2) pulsar receiver, and (3) tablet PC (Windows) (Fig. 16.9).

The target signal is compared with the reference signal and interpreted into acoustic impedance as:

$$Z(\text{target}) = \frac{1 - \frac{S(\text{target})}{S0}}{1 + \frac{S(\text{target})}{S0}} Z(\text{sub}) = \frac{1 - \frac{S(\text{target})}{S(\text{ref})} \cdot \frac{Z(\text{sub}) - Z(\text{ref})}{Z(\text{sub}) + Z(\text{ref})}}{1 + \frac{S(\text{target})}{S(\text{ref})} \cdot \frac{Z(\text{sub}) - Z(\text{ref})}{Z(\text{sub}) + Z(\text{ref})}} Z(\text{sub}) \quad (16.5)$$

where  $S0$  is the transmitted signal,  $S_{\text{target}}$  and  $S_{\text{ref}}$  are reflections from the target and reference, respectively, and  $Z_{\text{target}}$ ,  $Z_{\text{ref}}$ , and  $Z_{\text{sub}}$  are the acoustic impedances of the target, reference, and substrate, respectively [20].

**Fig. 16.8** A prototype of ultrasound stiffness checker. Figure is the whole system of the ultrasound stiffness checker



Finally, we can acquire the acoustic impedance of the targeted object on the tablet PC, based on the acoustic impedance of the reference.

## 16.3 Results

### 16.3.1 SAM Observation of PDL

Figure 16.10 is the result of the PC screen of SAM showing rat PDL. This result provided four visual information such as the sound speed intensity, the sound speed, the attenuation, and the sample thickness (Fig. 16.10a–d). SAM clearly visualized two-dimensional color distribution of the sound speed of both IRR and MRR (Fig. 16.11a, b). SAM also clearly visualized two-dimensional color distribution of the dentin and the alveolar bone. The gradation color table indicated the sound speed propagating in the sample. In the gradation color table, the lowest sound speed was 1,500 m/s, and the highest sound speed was 1,800 m/s (Fig. 16.11c).

IRR and MRR were composed of very low sound speed areas (blue) in 3-week-old postnatal group (Fig. 16.12a, e). In 5-week-old postnatal group, IRR and MRR were composed of low to middle sound speed areas (blue to green) (Fig. 16.12b, f).

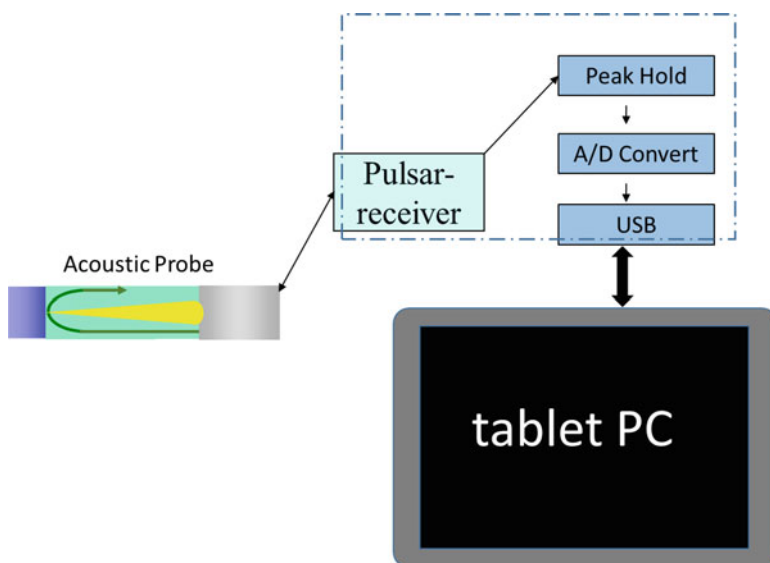


**Fig. 16.9** Block diagram of ultrasound stiffness checker

In a 7-week-old postnatal group, IRR and MRR were composed of middle sound speed areas (yellow to green) (Fig. 16.12c, g). In 10 weeks postnatal group, IRR and MRR were composed of middle to high sound speed areas (green) (Fig. 16.12d, h). The low sound speed area decreased, and middle sound speed areas gradually increased in both IRR and MRR depending on the rat growth.

### 16.3.2 Sound Speed Analysis

The mean value of sound speed propagating in each region was calculated. The sound speed of IRR and MRR is shown in Table 16.1. In IRR, there was no statistical difference between 3-week group and the 5-week group (3w 1,529 m/s  $\pm$  15.2 m/s vs. 5w 1,541 m/s  $\pm$  14.1 m/s;  $p=0.605$ ), between 5-week group and 7-week group (5w 1,541 m/s  $\pm$  14.1 m/s vs. 7w 1,563 m/s  $\pm$  18.2 m/s;  $p=0.169$ ), between 5-week group and 10-week group (5w 1,541 m/s  $\pm$  14.1 m/s vs. 10w 1,564 m/s  $\pm$  21.4 m/s;  $p=0.054$ ), and between 7-week group and 10-week group (7w 1,563 m/s  $\pm$  18.2 m/s vs. 10w 1,564 m/s  $\pm$  21.4 m/s;  $p=0.999$ ). However, the sound speed of IRR was significantly increased depending on the development (3w 1,529 m/s  $\pm$  15.2 m/s vs. 7w 1,563 m/s  $\pm$  18.2 m/s;  $p=0.012$  and 3w 1,529 m/s  $\pm$  15.2 m/s vs. 10w 1,564 m/s  $\pm$  21.4 m/s;  $p=0.002$ ). In MRR, there was no statistical difference between 3-week group and 5-week group (3w 1,536 m/s  $\pm$  16.1 m/s vs. 5w 1,556 m/s  $\pm$  18.4 m/s;  $p=0.125$ ), between 3-week group and 7-week group (3w 1,536 m/s  $\pm$  16.1 m/s vs. 7w 1,560 m/s  $\pm$  15.7 m/s;  $p=0.063$ ), between 5-week group and 7-week group

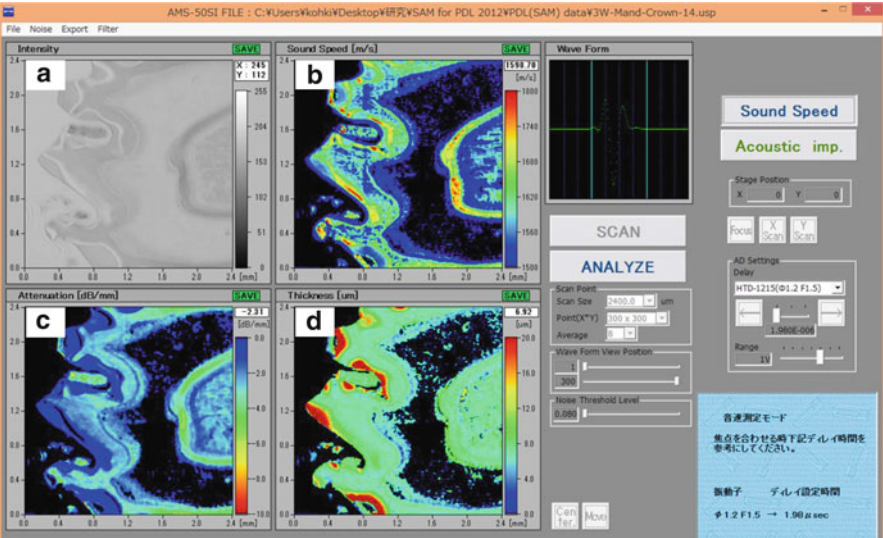


**Fig. 16.10** PC screen of SAM image of PDL. Two-dimensional color distribution with the resolution of the 2.4×2.4 mm sample area is visualized with 300×300 pixels. (a) sound speed intensity image, (b) sound speed image, (c) attenuation image, and (d) sample thickness image

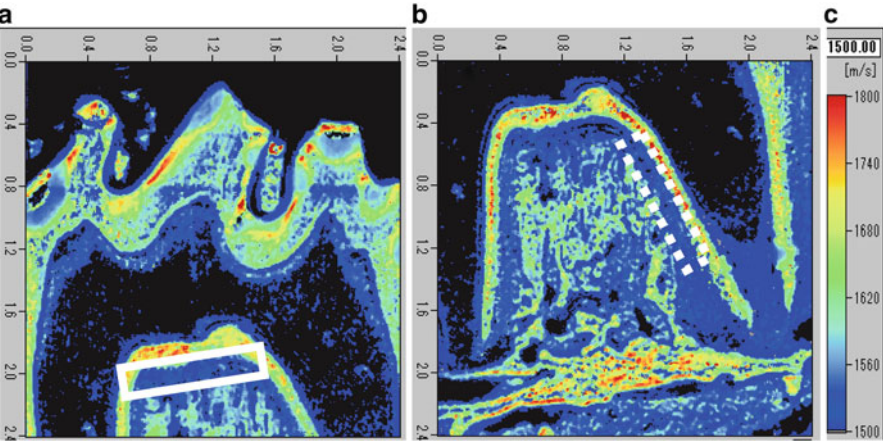


**Fig. 16.11** SAM image of IRR. IRR is encircled by the *solid rectangle* (a). SAM image of MRR. MRR is encircled by the *dotted rectangle* (b). The color graduation table of the sound speed (c)

(5w 1,556 m/s±18.4 m/s vs. 7w 1,560 m/s±15.7 m/s;  $p=0.974$ ), between 5-week group and 10-week group (5w 1,556 m/s±18.4 m/s vs. 10w 1,566 m/s±16.9 m/s;  $p=0.583$ ), and between 7-week group and 10-week group (7w 1,560 m/s±15.7 m/s vs. 10w 1,566 m/s±16.9 m/s;  $p=0.881$ ). However, the sound speed of MRR was

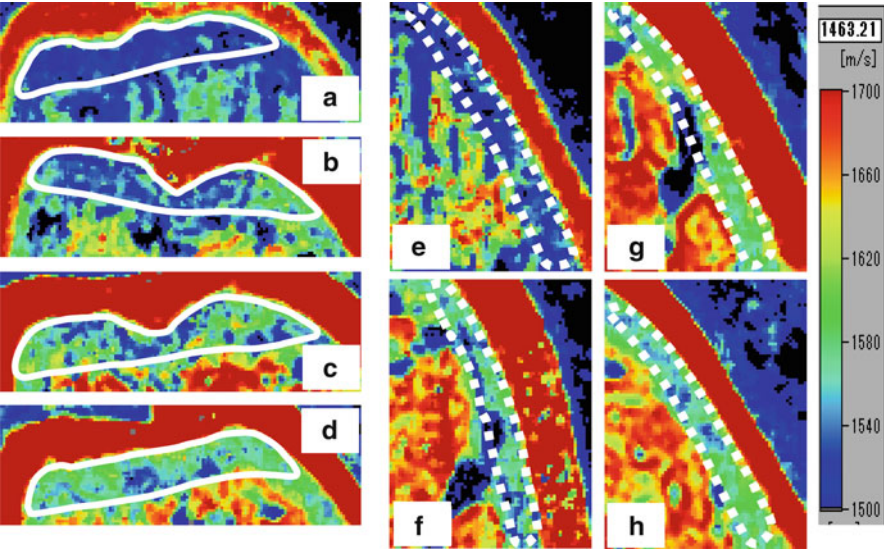


**Fig. 16.12** SAM images of IRR (a–d) and MRR (e–h). 3-week-old (a, e). 5-week-old (b, f). 7-week-old (c, g). 10-week-old (d, h)

**Table 16.1** Mean sound speed propagating in IRR and MRR, respectively, and standard deviations between IRR and MRR. Statistic evaluation was performed by one-way ANOVA and Tukey’s method, or by paired *t*-test

	IRR(m/s)	sMRR(m/s)
3w	1,529±15.2 <sup>a,b</sup>	1,536±16.1 <sup>c</sup>
5w	1,541±14.1 <sup>d</sup>	1,556±18.4 <sup>d</sup>
7w	1,563±18.2 <sup>a</sup>	1,560±15.7
10w	1,564±21.4 <sup>b</sup>	1,566±16.9 <sup>c</sup>

<sup>a,b</sup>*P*<0.01 by one-way ANOVA and Tukey’s method  
<sup>c</sup>*P*<0.05 by one-way ANOVA and Tukey’s method  
<sup>d</sup>*P*<0.05 by paired *t*-test

significantly increased depending on the development (3w 1,536 m/s±16.1 m/s vs. 10w 1,566 m/s±16.9 m/s; *p*=0.003).

There was significant difference between IRR and MRR in 5-week group (IRR 1,541 m/s±14.1 m/s vs. MRR 1,556 m/s±18.4 m/s; *p*=0.003).

**16.3.2.1 AIM Observation of Dentin Caries**

Figure 16.13 is the result of the PC screen of AIM showing dentin caries. This result provided two visual information, the acoustic intensity (Fig. 16.13a) and the acoustic impedance (Fig. 16.13b). In the acoustic impedance image, AIM clearly visualized two-dimensional color distribution of the acoustic impedance of the sound



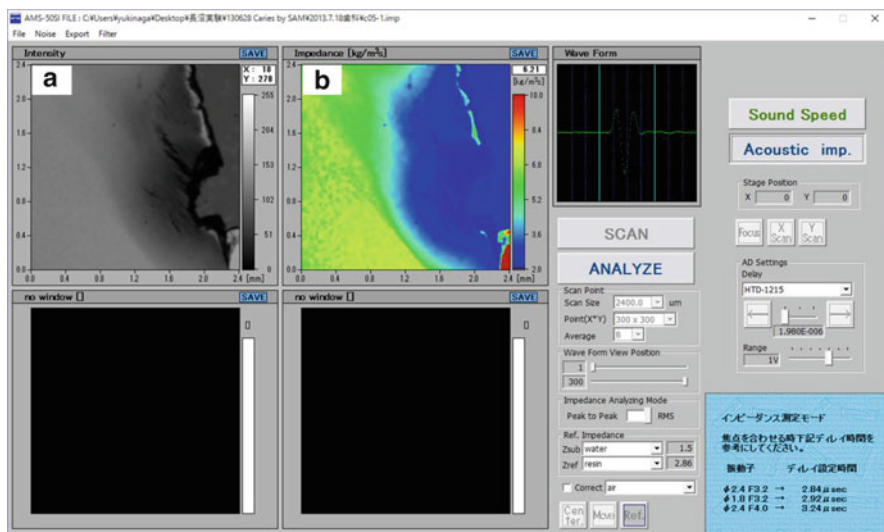


**Fig. 16.13** PC screen of AIM image of dentin caries. Two-dimensional color distribution with the resolution of the  $2.4 \times 2.4$  mm sample area is visualized with  $300 \times 300$  pixels. Acoustic intensity image (a), acoustic impedance (b) image

dentin as well as the dentin caries. The gradation color of the dentin caries (Fig. 16.14a) differed from that of the sound dentin (Fig. 16.14b). The dentin caries was composed of low acoustic impedance areas (blue to light blue). However, the sound dentin was composed of higher acoustic impedance areas (green to yellow) than the carious dentin lesion. The comparison of the acoustic impedance of both sound dentin and dentin caries is shown in Fig. 16.15. The acoustic impedance of the dentin caries was significantly lower than that of the sound dentin (sound dentin vs. dentin caries;  $6.75 \pm 0.14$  kg/m<sup>2</sup>s vs.  $2.47 \pm 0.41$  kg/m<sup>2</sup>s;  $p = 2.29 \times 10^{-12}$ ).

### 16.3.2.2 SEM Observation of Dentin Caries

SEM images are shown in Fig. 16.16. The sound dentin areas showed smooth surface, and the transverse sections of dentinal tubules were aligned regularly (Fig. 16.16a). However, surface erosion and destruction were detected on the dentin caries. The dentinal tubules were aligned irregularly, and the cross sections of dentinal tubules showed wider and narrower on the dentin caries than those on the sound dentin (Fig. 16.16b).

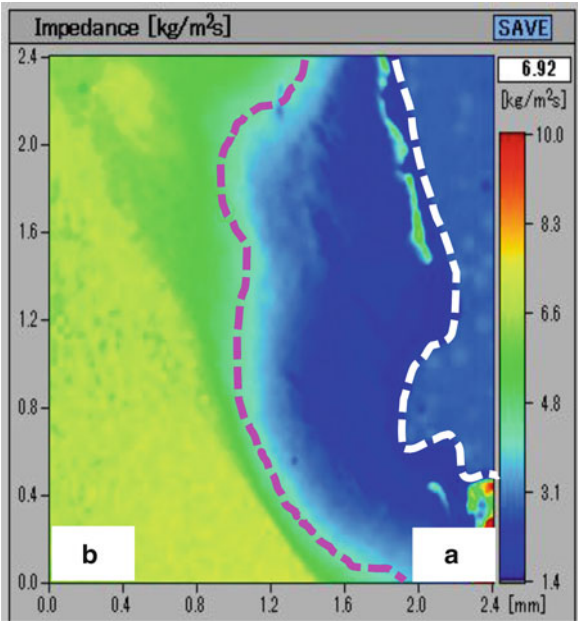


**Fig. 16.14** Acoustic impedance image of the carious dentin lesion. Sound dentin area consists of higher acoustic impedance area (*green to yellow*) (a). Dentin caries consists of low acoustic impedance area (*light blue to blue*) (b)

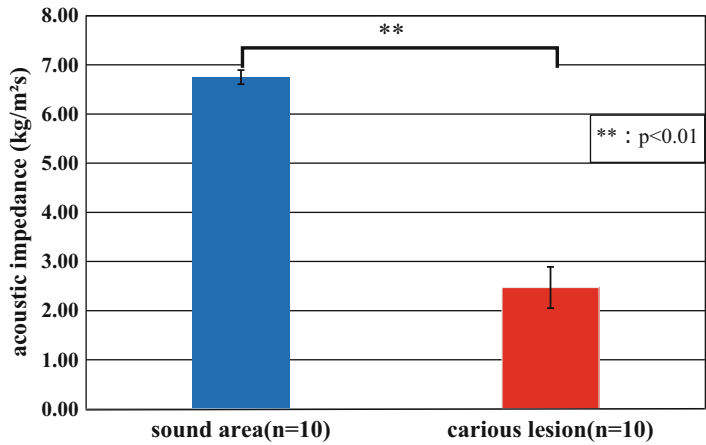


**Fig. 16.15** Bar graph of the acoustic impedance between sound dentin area and carious dentin lesion. *Blue bar* is the mean acoustic impedance of sound dentin. *Red bar* is the mean acoustic impedance of dentin caries



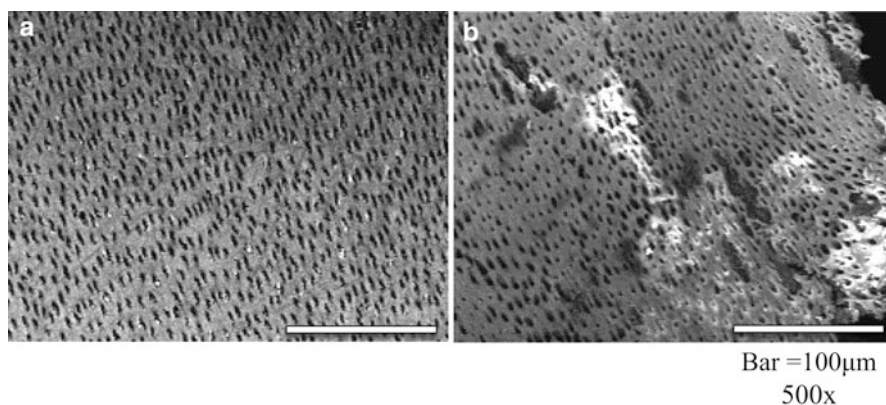


**Fig. 16.16** SEM images of sound dentin (a) and dentin caries (b). 500×original magnification. Bar=100 μm

### 16.3.3 Ultrasound Stiffness Checker

Figure 16.17 shows the actual measurement of human sound tooth. Since the probe surface is flat, it is difficult to measure the dental carious cavity. Many improvements are necessary to apply the diagnosis for dental caries.

## 16.4 Discussion

### 16.4.1 SAM Observation of PDL

In the present study, our SAM clearly visualized the gradation color images and distribution of rat PDL. SAM images were equal to histological appearances obtained by light microscopy. These results are the first time that SAM is applied to investigate the elastic property of PDL.

Previous studies reported that the elastic property of PDL was decreased along with development [28–31]. In *in vivo* studies, the elastic property of PDL were investigated by the displacement of the rat molar under the mechanical loads [28, 31] and the measurement of the load by pushing the rat incisor out of alveolar socket [29, 30]. However, these methods measured not only the elastic property of PDL but also the elastic property of alveolar bone. Meanwhile, in *in vitro* studies, numerical analyses using finite element model (FEM) study did not precisely reflect the elastic property of PDL [32, 33], because the occlusal conditions are not fully considered.

In the present study, the sound speed propagating in PDL was significantly increased in a course of development. These results indicate that the elasticity of PDL is decreased along with rat development; in other words PDL becomes harder during development. Previous studies reported that collagens such as type I, III, and



**Fig. 16.17** Actual examination of human teeth. Ultrasound stiffness checker shows the ultrasound impedance of the tooth in the yellow circle

XII collagen were implicated in the regulation of the development and/or maturation of PDL [34–36]. And other previous studies reported that non-collagens such as fibroblast growth factor (FGF), alkaline phosphatase, and connective tissue growth factor (CCN/CTGF) were implicated in the regulation of the development and/or maturation of PDL [36–38]. Therefore, the present study indicates that the extracellular matrix molecules may play a pivotal role to regulate the elasticity of PDL.

Previous studies reported that occlusal force influence to mature PDL [35, 39]. In a study, the occlusal forces induced to promote the collagens synthesis [35]. In another study, the occlusal forces induced to express insulin-like growth factor-1. These collagens and growth factor had influence on the development and/or maturation of PDL [39]. In the present study, MRR elasticity was lower than IRR elasticity in 5-week-old. We speculate that in order to resist the lateral loading of occlusal force MRR became harder to bind firmly between the tooth root and the alveolar bony socket.

The present study indicates that the decreased elasticity of PDL is induced by the morphological development such as the production of collagen(s) and/or proteoglycan(s) and the functional development such as the occlusal construction and/or the development of the masticatory muscles.

SAM is a powerful tool for evaluating the elasticity and its distribution in the targeted tissues *in situ*. This study suggests that the increased elasticity of PDL is one of the developmental processes of the periodontal tissues.

### 16.4.2 AIM Observation of Dentin Caries

To date, AIM has been mainly applied for the observation of soft tissues such as synovial membrane [13] and coronary artery [20]. In the present study, AIM was able to clearly visualize the color distribution of the acoustic impedance of both the sound and carious dentin. Moreover, AIM enabled to evaluate the elastic property calculating the acoustic impedance of the sample. Taken together these results, we propose that AIM may be useful to diagnose the dental caries visually and numerically.

Previous study reported that the Vickers hardness of the carious dentin lesion was significantly lower than that of the sound dentin areas [40]. In the present study, the acoustic impedance of the carious dentin lesion was significant lower than in the sound dentin area. The Vickers hardness test is a destructive examination; therefore, there are limitations to apply the measurement of the Vickers hardness to diagnose human caries. The ultrasonic testing is a nondestructive examination, so the calculation of the acoustic impedance of the dentin caries may be a noninvasive and safe method to diagnose human caries.

SEM observation revealed that caries induced microstructural deterioration of dentin. This result suggested that acid produced by oral bacterial metabolism decalcified the Ca element included in dentin.

To understand the elastic property due to the pathological change is important information to diagnose the disease in medicine and dentistry. It has been well known that caries make dentin soft. But, unfortunately, it has not established to evaluate precisely the elasticity of the carious dentin. In the present study, AIM enabled to visualize the dentin caries clearly and evaluate it numerically. Based on the principle of AIM, we are going to complete a novel portable acoustic caries detector.

**Acknowledgments** We wish to thank Mr. Katsuyoshi Shoji, Department of Orthopaedic Surgery, Tohoku University Graduate School of Medicine, for his excellent assistance. This work was supported by MEXT KAKENHI Grant Number JP25462982.

## References

1. Saijo Y, Tanaka M, Okawai H, Dunn F. The ultrasonic properties of gastric cancer tissues obtained with a scanning acoustic microscope system. *Ultrasound Med Biol.* 1991;17:709–14.
2. Sasaki H, Tanaka M, Saijo Y, et al. Ultrasonic tissue characterization of renal cell carcinoma tissue. *Nephron.* 1996;74:125–30.
3. Saijo Y, Tanaka M, Okawai H, Sasaki H, Nitta SI, Dunn F. Ultrasonic tissue characterization of infarcted myocardium by scanning acoustic microscopy. *Ultrasound Med Biol.* 1997;23:77–85.
4. Sasaki H, Saijo Y, Tanaka M, et al. Acoustic properties of dialysed kidney by scanning acoustic microscopy. *Nephrol Dial Transplant Off Publ Eur Dial Transplant Assoc – Eur Ren Assoc.* 1997;12:2151–4.

5. Saijo Y, Sasaki H, Okawai H, Nitta S, Tanaka M. Acoustic properties of atherosclerosis of human aorta obtained with high-frequency ultrasound. *Ultrasound Med Biol.* 1998;24:1061–4.
6. Saijo Y, Sasaki H, Sato M, Nitta S, Tanaka M. Visualization of human umbilical vein endothelial cells by acoustic microscopy. *Ultrasonics.* 2000;38:396–9.
7. Saijo Y, Ohashi T, Sasaki H, Sato M, Jorgensen CS, Nitta S. Application of scanning acoustic microscopy for assessing stress distribution in atherosclerotic plaque. *Ann Biomed Eng.* 2001;29:1048–53.
8. Sasaki H, Saijo Y, Tanaka M, Nitta S. Influence of tissue preparation on the acoustic properties of tissue sections at high frequencies. *Ultrasound Med Biol.* 2003;29:1367–72.
9. Saijo Y, Miyakawa T, Sasaki H, Tanaka M, Nitta S. Acoustic properties of aortic aneurysm obtained with scanning acoustic microscopy. *Ultrasonics.* 2004;42:695–8.
10. Sano H, Saijo Y, Kokubun S. Material properties of the supraspinatus tendon at its insertion- a measurement with the scanning acoustic microscopy. *J Musculoskelet Res.* 2004;8:29–34.
11. Saijo Y, Sasaki H, Hozumi N, Kobayashi K, Tanaka M, Yambe T. Sound speed scanning acoustic microscopy for biomedical applications. *Technol Health Care: Off J Eur Soc Eng Med.* 2005;13:261–7.
12. Hozumi N, Yamashita R, Lee CK, et al. Time-frequency analysis for pulse driven ultrasonic microscopy for biological tissue characterization. *Ultrasonics.* 2004;42:717–22.
13. Hagiwara Y, Saijo Y, Chimoto E, et al. Increased elasticity of capsule after immobilization in a rat knee experimental model assessed by scanning acoustic microscopy. *Ups J Med Sci.* 2006;111(3):303–13.
14. Sano H, Hattori K, Saijo Y, Kokubun S. Does decalcification alter the tissue sound speed of rabbit supraspinatus tendon insertion? In vitro measurement using scanning acoustic microscopy. *Ultrasonics.* 2006;44:297–301.
15. Berkowitz BKB, Holland GR, Moxham BJ. Periodontal ligament. In: Berkowitz BKB, Holland GR, Moxham BJ, editors. *Oral anatomy, histology and embryology.* 3rd ed. London: Mosby; 2007. p. 180–204.
16. Kaku M, Yamauchi M. Mechano-regulation of collagen biosynthesis in periodontal ligament. *J Prosthodont Res.* 2014;58:193–207.
17. Komatsu K. Mechanical strength and viscoelastic response of the periodontal ligament in relation to structure. *J Dent Biomech.* 2010;2010:502318.
18. Komatsu K, Chiba M. The effect of velocity of loading on the biomechanical responses of the periodontal ligament in transverse sections of the rat molar in vitro. *Arch Oral Biol.* 1993;38(5):369–75.
19. Komatsu K, Kanazashi M, Shimada A, Shibata T, Viidik A, Chiba M. Effects of age on the stress-strain and stress-relaxation properties of the rat molar periodontal ligament. *Arch Oral Biol.* 2004;49(10):817–24.
20. Saijo Y, Hozumi N, Kobayashi K, et al. Ultrasound speed and impedance microscopy for in vivo imaging. Conference proceedings: annual international conference of the IEEE engineering in medicine and biology society IEEE engineering in medicine and biology society conference 2007. 2007:1350–3.
21. Kobayashi K, Yoshida S, Saijo Y, Hozumi N. Acoustic impedance microscopy for biological tissue characterization. *Ultrasonics.* 2014;54:1922–8.
22. Gunawan AI, Hozumi N, Yoshida S, Saijo Y, Kobayashi K, Yamamoto S. Numerical analysis of ultrasound propagation and reflection intensity for biological acoustic impedance microscope. *Ultrasonics.* 2015;61:79–87.
23. Usha CSR. Dental caries – a complete changeover (part I). *J Conserv Dent.* 2009;12(2):46–54.
24. Shimizu A, Nakashima S, Nikaido T, Sugawara T, Yamamoto T, Momoi Y. Newly developed hardness testing system, “Cariotester”: measurement principles and development of a program for measuring knoop hardness of carious dentin. *Dent Mater J.* 2013;32(4):643–7.
25. Kodaka T, Debari K, Yamada M. Correlation between microhardness and mineral content in sound human dentin. *J Showa Univ Dent Soc.* 1998;18(2):199–201.

26. O'Brien Jr WD, Olerud J, Shung KK, Reid JM. Quantitative acoustical assessment of wound maturation with acoustic microscopy. *J Acoust Soc Am*. 1981;69(2):575–9.
27. Saijo Y, Okawai H, Sasaki H, et al. Evaluation of the inner-surface morphology of an artificial heart by acoustic microscopy. *Artif Organs*. 2000;24(1):64–9.
28. Picton DC, Wills DJ. Viscoelastic properties of the periodontal ligament and mucous membrane. *J Prosthet Dent*. 1978;40(3):263–72.
29. Yamane A. The effect of age on the mechanical properties of the periodontal ligament in the incisor teeth of growing young rats. *Gerodontology*. 1990;9(1):9–16.
30. Pini M, Wiscott HW, Scherrer SS, Botsis J, Belser UC. Mechanical characterization of bovine periodontal ligament. *J Periodontal Res*. 2002;37(4):237–44.
31. Kavarizadeh A, Bourauel C, Jager A. Experimental and numerical determination of initial tooth mobility and material properties of the periodontal ligament in rat molar specimens. *Eur J Orthod*. 2003;25(6):569–78.
32. Komatsu K. In vitro mechanics of the periodontal ligament in impeded and unimpeded rat mandibular incisors. *Arch Oral Biol*. 1988;32(4):249–55.
33. Chiba M, Yamane A, Oshima S, Komatsu K. In vitro measurement of regional differences in the mechanical properties of the periodontal ligament in the rat incisor. *Arch Oral Biol*. 1990;35(2):153–61.
34. Huang YH, Ohsaki Y, Kurisu K. Distribution of type I and III collagen in the developing periodontal ligament of mice. *Matrix*. 1991;11(1):25–35.
35. Karimbux NY, Rosenblum ND, Nishimura I. Site-specific expression of collagen I and XII mRNA in the rat periodontal ligament at two developmental stages. *J Dent Res*. 1992;71(7):1355–62.
36. Ozaki S, Kaneko S, Podyma-Inoue KA, Yanagishita M, Soma K. Modulation of extracellular matrix synthesis and alkaline phosphatase activity of periodontal ligament cells by mechanical stress. *J Periodontal Res*. 2005;40(2):110–7.
37. McCulloch CA, Bordin S. Role of fibroblast subpopulations in periodontal physiology and pathology. *J Periodontal Res*. 1991;26(3):144–54.
38. Asano M, Kubota S, Nakanishi T, Nishida T, Yamaai T, Yosimichi G, Ohyama K, Sugimoto T, Murayama Y, Takigawa M. Effect of connective tissue growth factor (CCN/CTGF) on proliferation and differentiation of mouse periodontal ligament-derived cells. *Cell Commun Signal*. 2005;5(3):11.
39. Termsuknirandorn S, Hosomichi J, Soma K. Occlusal stimuli influence on the expression of IGF-1 and the IGF-1 receptor in the rat periodontal ligament. *Angle Orthod*. 2008;78(4):610–6.
40. Oikawa M, Itoh K, Kusunoki M, Kitanaka N, Hasegawa T. Comparison of rotary and ultrasonic caries removal determined by two fluorescent caries detection devices. *Jpn J Conserv Dent*. 2013;56(1):78–84.

**Open Access** This chapter is distributed under the terms of the Creative Commons Attribution 4.0 International License (<http://creativecommons.org/licenses/by/4.0/>), which permits use, duplication, adaptation, distribution and reproduction in any medium or format, as long as you give appropriate credit to the original author(s) and the source, provide a link to the Creative Commons license and indicate if changes were made.

The images or other third party material in this chapter are included in the work's Creative Commons license, unless indicated otherwise in the credit line; if such material is not included in the work's Creative Commons license and the respective action is not permitted by statutory regulation, users will need to obtain permission from the license holder to duplicate, adapt or reproduce the material.

